THE ASTROPHYSICAL JOURNAL, 440:706–721, 1995 February 20

THE THREE-DIMENSIONAL STRUCTURE OF THE CASSIOPEIA A SUPERNOVA REMNANT. I. THE SPHERICAL SHELL

JERI E. REED
Department of Physics and Astronomy, Arizona State University, Tempe, AZ 85287;
also Turku University, Tuorla Observatory, Finland
E-mail: jer@wfpc3.la.asu.edu

J. JEFF HESTER
Department of Physics and Astronomy, Arizona State University, Tempe, AZ 85287
E-mail: jjh@wfpc.la.asu.edu

A. C. FABIAN
Institute of Astronomy, Madingley Road, Cambridge, England CB3 0HA
E-mail: acf@mail.ast.cam.ac.uk

AND

P. F. WINKLER
Department of Physics, Middlebury College, Middlebury, VT 05753
E-mail: winkler@midd.cc.middlebury.edu
Received 1994 June 6; accepted 1994 September 2

ABSTRACT

The three-dimensional structure of the Cassiopeia A supernova remnant is explored via 73 long-slit optical spectra (spanning 6250–7600 Å) which cross the face and "jet" region of the nebula. We extracted position, radial velocity, and line intensity information from nearly 25,000 cross sections of these original data, resulting in a library of 3663 fast-moving knots (FMKs) and 450 quasi-stationary flocculi (QSFs) detections. We performed an iterative least-squares spherical fit to the data, using this to convert radial velocities to line-of-sight distances.

We have built up a picture of the remnant as a spherical circumstellar shell of $104\farcs5 \pm 0\farcs7$ radius, corresponding to 5.3×10^{18} cm (1.7 pc). The center on the sky is displaced by $8\farcs7$ west and $12\farcs6$ north of the proper motion center. The velocity center of our fitted sphere has been redshifted by 770 ± 40 km s^{-1} from the presumed expansion center at zero velocity. This expansion of the ejecta from a displaced center accounts for the observed radial velocity difference at the front and back faces. The average rate of expansion of the FMKs is 5290 ± 90 km s^{-1}, while the asymmetric values are 4520 km s^{-1} at the blueshifted face, and 6060 km s^{-1} at the redshifted face. Based on a comparison of our suite of radial velocities with all the available proper-motion and age data, we find the distance to Cas A to be $3.4^{+0.3}_{-0.1}$ kpc. Our kinematic analysis shows the optically emitting ejecta of Cas A have been slowed certainly by less than 7%, and probably by less than 4% and that the velocity of the reverse shock driven into the knots is about 200 km s^{-1}. We conclude that the center of expansion of the supernova is displaced by about 0.36 pc (1.1×10^{18} cm) to the northwest and front of the geometric center of the bubble. The geometry suggests that the density of the surrounding medium is greater in the direction of displacement. The asymmetrically distributed radial velocities of the QSFs, of which 76% are blueshifted, also support this interpretation.

Line ratios suggest that the pressure is higher on the front side of the remnant than on the back. There is a global trend of increasing electron density with radial velocity in this direction, and a stronger trend of increasing [O II]/[S II] from back to front. We suggest that this is due to collisional deexcitation of [S II] on the high-pressure side of the remnant, rather than a real composition trend. We also see evidence for density variations in both the shell and ejecta, concluding that the front face of the composite shell is of higher density than the far face, and that the blueshifted ejecta *may* be of higher density than that at the far face. However, in this study we see no evidence for any ordered change in abundances of the ejecta across Cas A.

The weight of observational evidence suggests that the general form of the Cas A supernova remnant is due to the expansion of ejecta from a displaced center within an approximately spherical shell. We have concluded that there is no optical evidence for a dual-hemisphere model in the velocity structure of Cas A. In particular, we find that the outer radio emission must truly lie outside the inner radio and optical shell. The inner shell is made up of decelerated circumstellar material and the SN material which was ejected at highest velocity. The optical FMKs consist of newly interacting knots of ejecta which are just undergoing deceleration and are distributed in rings on the surface of the sphere.

Subject headings: ISM: individual (Cassiopeia A) — ISM: kinematics and dynamics — ISM: structure — supernova remnants

1. INTRODUCTION

Cassiopeia A is the youngest known Galactic supernova remnant and is famous for the wide range of line ratios seen in its knots of optical emission. Cas A spans 4′ on the sky, corresponding to a physical diameter of 3–4 pc depending on the distance adopted. The supernova which gave rise to Cas A was probably observed by Flamsteed in 1680, an observation which was misunderstood and lost in a transcription of star catalogs in the early 18th century (Ashworth 1980) but found again after Cas A was rediscovered in 1948 as the brightest nonthermal radio source other than the Sun (Ryle & Smith 1948). Cas A is also a strong X-ray source and has been observed extensively in various wavebands over nearly four decades (e.g., in the optical: Baade & Minkowski 1954; Minkowski 1959; van den Bergh & Dodd 1970; Kamper & van den Bergh 1976; van den Bergh & Kamper 1983, hereafter VDBK83; van den Bergh & Kamper 1985, hereafter VDBK85; in the radio: Bell 1976; Tuffs 1986; Braun, Gull, & Perley 1987; Anderson & Rudnick 1995; and in the X-ray: Fabian et al. 1980; Jansen et al. 1988). Cas A is now thought to be the debris of a very massive, late-type WN star which exploded as a Type II supernova (Fesen, Becker, & Blair 1987). Its apparently low luminosity at the time of explosion, and the small size of the remnant, suggest that it exploded as a blue giant (Chevalier 1976), similar to SN 1987A. At radio and X-ray wavelengths, the remnant appears as an approximately circular region of diffuse emission which surrounds an inner bright ring of clumpy emission. The circular region has a protrusion at the northeast, which is aligned with a break in the inner emission. The optical emission in the remnant comes from a smaller number of clumps at the inner radius, which are concentrated in the north, and is also seen as a few patchy filaments to the NE, constituting the "jet," at about 3′ radius.

Three types of optical emission have been observed, which differ kinematically and in composition. The fast-moving knots (FMKs) have spatial velocities of about 5000 km s^{-1} for the bulk of the emission and up to 11,000 km s^{-1} in the outer filaments (Fesen, Becker, & Goodrich 1988). Some of the FMKs emit solely oxygen lines, while others have varying relative emission in oxygen and the products of oxygen-burning such as sulfur, argon, and calcium. None of them shows emission from hydrogen, helium, or nitrogen (Peimbert & van den Bergh 1971; Peimbert 1971; Kirshner & Chevalier 1977; Chevalier & Kirshner 1978, 1979). New emission continues to appear, filling in regions at the inner radius (VDBK83). FMKs have been known to be ejecta since not long after their discovery (Minkowski 1959). Cas A also has slow-moving knots (known as quasi-stationary flocculi, or QSFs), which have space velocities of about 200 km s^{-1}, on average, but show considerable variation. These emit Hα, strong lines of nitrogen, and sometimes [O I], with the ratio of the summed N II to Hα strengths being ~1.3–5.0, or N/H abundances estimated as 3–10 times the cosmic abundance (Chevalier & Kirshner 1978). The QSFs are thought to be the remains of the outer layers of the progenitor star which were entirely or almost entirely removed in episodes of mass loss predating the star's explosion (e.g., van den Bergh 1971; Fesen et al. 1987). Nitrogen or hydrogen emission has been seen in only 15 knots of high velocity, suggesting that possibly a thin photospheric skin of hydrogen remained at the time of the star's explosion. Because these few knots move like FMKs, but have the composition of QSFs, they were called fast-moving flocculi, or FMFs (Fesen et al. 1987). These distinct classes of emission have led to speculation that Cas A has preserved some of its presupernova layered structure in its expanding ejecta. Nevertheless, detailed spectroscopic studies of a few of the knots have revealed no relationship between composition and velocity, although it has been suggested that sulfur-rich knots, presumably from deep within the stellar interior, may actually be expanding faster than oxygen-rich knots of lighter composition (Chevalier & Kirshner 1979; VDBK83), suggesting that some mixing of the layers of the progenitor may have occurred. An immediate question is whether enough of an overall pattern remains in the ejecta for us to unscramble today's Cas A and understand something more of its evolution. With its accessible angular size, recent date of explosion, and fascinatingly varied types of emission, Cas A presents an opportunity to study the composition and early behavior of a supernova remnant which may only be equaled as SN 1987A unfolds. Yet clearly, Cas A is so complex that only a comprehensive study of its emission can hope to answer questions about the current distribution of ejecta and the nature of the circumstellar environment. In the following studies, we present the results of such a survey, which are based on the most extensive set of radial velocity data yet analyzed. The preliminary analysis of this set has already shown that the FMKs of Cas A form large, unexpected rings of emission on a spherical shell (Reed, Winkler, & Fabian 1989; Reed et al. 1991). In the current report, we will concentrate on the kinematic and global aspects of Cas A, as evidenced by its optical FMKs. These lead us to new insights into the three-dimensional structure of the remnant, the nature of the circumstellar environment, and to a refinement of Cas A's estimated distance from us. In a subsequent work, (Reed, Hester, & Winkler 1995 hereafter Paper II), we will explore the detailed distribution of the optical emission, and the nature of the optical rings.

In § 2, we outline our observations, the standard reduction of the spectral images, and the nonstandard extraction of position, velocity, and flux information for the FMKs. In § 3 we discuss the implications of the data for the three-dimensional structure of Cas A and also show that the remnant is well described by a spherical shell. We also consider the implications of the data for distance estimates to Cas A. In § 4 we extend our picture to explore the immediate environment around Cas A. We also explore the competing effects of true abundance differences and collisional pressures on the line ratios in Cas A, adding information about trends of composition and density to the total picture. Section 5 summarizes our findings.

2. OBSERVATIONS AND DATA ANALYSIS

2.1. *Observations*

Optical long-slit spectra covering the face of Cas A were taken by A. C. F. and P. F. W. using the Intermediate Dispersion Spectrograph (IDS) and 235 mm camera on the 2.5 m Isaac Newton telescope at La Palma during 1986 September 28–30. The CCD detector used was a GEC chip consisting of 22 μm pixels in a 385 × 576 array. The slit was 221″ by 2.″5, with pixels of 0.″64 in the spatial dimension. We obtained 73 spectra, 61 of which were taken with the slit oriented north/south. These are spaced by 4″, so that coverage of the face of the remnant is 63%, with gaps between spectra of 1.″5. The 12 east/west oriented spectra are important, because in crossing the north/south observations they confirm the positions of

knots of emission both on the sky and in velocity space. The pattern of the spectra is shown superposed on a deep CCD image of Cas A in Figure 1. This underlying [O II] $\lambda\lambda$7320, 7330 image was taken on the 4 m telescope at Kitt Peak National Observatory in 1986 September and is therefore contemporary to the spectroscopic observations. The filter bandpass was 200 Å centered at 7350 Å, passing the full range of high-velocity emission from Cas A. The wavelength range covered in our spectra was from 6250 to 7600 Å with a wavelength resolution of 2.3 Å pixel^{-1}, and the instrumental line resolution was 9 Å FWHM, corresponding to 390 km s^{-1}. The velocity width of the vast majority of knots is less than this, so they are therefore unresolved. The accuracy of the central velocity observed for a knot is limited by the slit width, since the placement of the knot in the slit can vary over $\pm$1.″75 corresponding to $\pm$2 pixels or $\pm$200 km s^{-1}. The spectral range included the lines of [N II], and Hα, characteristic of the QSF, and [O I], [S II], [Ar III], and [O II], typically found in FMKs. The wavelength resolution was sufficient to resolve the [O II] $\lambda\lambda$7320, 7330 and [S II] $\lambda\lambda$6717, 6731 doublets.

The integration time for each spectrum was 1000 s, and typical seeing ranged from 0.″9 to 1.″1. Observations from the last part of the third night have the highest background levels due to thin clouds. These are the east/west oriented spectra. We calibrated the data in wavelength using CuNeAr and CuNe standard lamps, with observations taken, on average, after every fifth data frame. The data were binned linearly in wavelength using a first-order fit to the bracketing calibration observations. The wavelength dispersion is extremely stable throughout the three nights. We fitted 22 lines for each CuNeAr spectrum and 14 lines for the three CuNe spectra. These arc lines range from an argon line at 6305 Å to a copper line at 7535 Å. The rms wavelength calibration error was 0.35 Å for the CuNe and 0.55 Å for the CuNeAr spectra. The CCD frames were bias-subtracted using an average bias frame. The GEC chip required a preflash to alleviate problems with deferred charge, and this pattern was also subtracted. Each frame was divided by a normalized flat-field frame created from tungsten dome flats.

We selected up to eight areas of each image which were judged to be free of emission from knots of ejecta, continua, or cosmic rays and averaged these to form a background spectrum which we subtracted row by row from the entire image. The background spectrum is later used to compile signal-to-noise ratio statistics for the image. Because of the patchy nature of the emission, we did not use any automatic cleaning program to remove cosmic-ray events. These were later flagged in our own analysis program and checked by hand.

Calibration sources were chosen from white dwarfs in the list of Oke & Gunn (1982; 1983) and were observed at the beginning and end of each night. Spline fits were used to interpolate between the tabulated values and also to create a smoothed spectrum from our observed calibration sources. The rms flux variation at the center of the spectral range was 8% over the course of one night and 11% over the course of the run, suggesting that the absolute calibration was accurate to

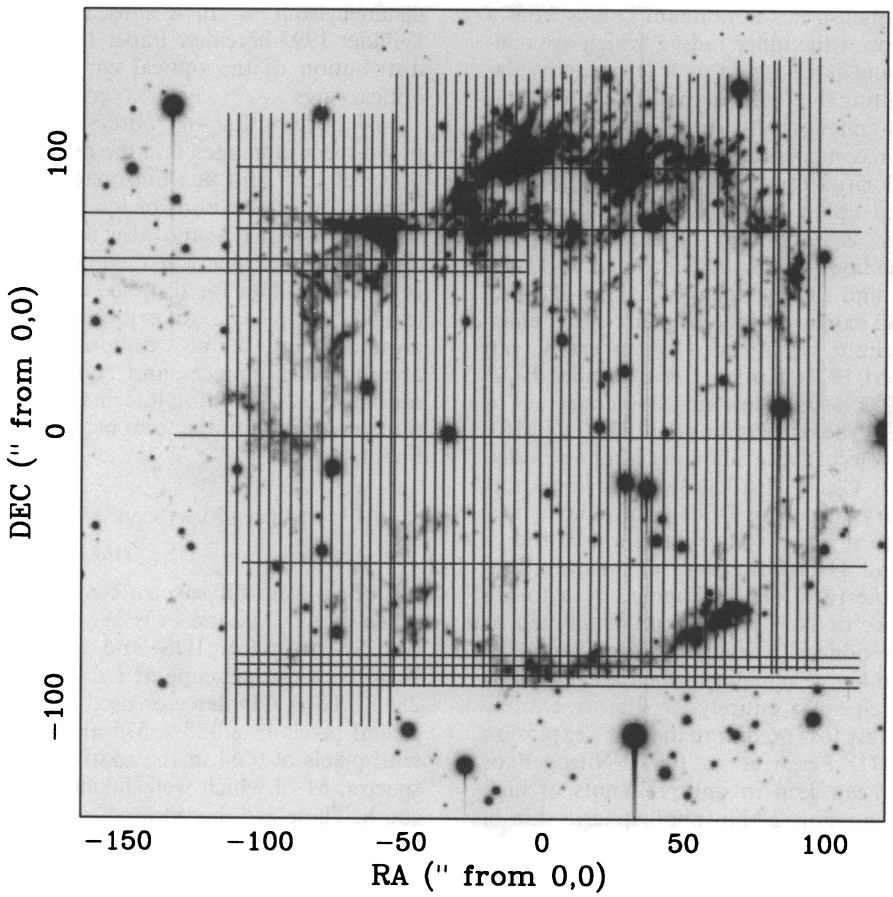

FIG. 1.—Map of the area of Cas A covered in our spectroscopic survey. The pattern of the spectra is shown superposed on a narrow-band [O II] λ7325 CCD image of Cas A, which dates from the same time as the spectroscopic data.

about $\pm 10\%$. We also looked at the response in different regions of the chip and found that the systematic variation was no more than the noise level between measurements. We corrected for atmospheric extinction as a function of hour angle for the observations. In addition, Cas A is highly reddened, and we corrected for this effect using the value $A_V = 4.3$ mag as found in Searle (1971).

We determined a value for the background level for every sky-subtracted image and used this to estimate the signal-to-noise ratio of the frame. We used the rows which had already been judged free of emission and used in the sky subtraction. An average spectrum created from this set of rows within the final sky-subtracted and calibrated image became the background spectrum for that image. The noise as a function of wavelength was larger in the positions of the night sky lines, but examination of the background spectrum showed this to be a small effect. The standard deviation about the mean value gives us a noise estimate for each image.

2.2. *Extraction of Velocities, Fluxes, and Positions*

Analysis of the spectral data includes three determinations: finding the radial velocity of each optical emission knot, finding the spectral lines and estimating the flux of each, and finding the position of each knot in right ascension and declination on the sky.

To accomplish the first two tasks, we developed an automated program to search our images for emission via a cross-correlation technique. Each image was examined cross section by cross section, that is, the spectrum corresponding to each pixel along the slit was searched separately for any optical emission, as we describe below. This amounted to some 25,000 one-dimensional spectra in total. In the automated program, the positions of the knots were recorded as the image number and pixel in which the emission was found. Emission at several different velocities is commonly present in a spectrum, and this is further complicated by the possible presence of both FMK and QSF emission, with their widely differing compositions. Two example spectra of moderate flux are shown in Figure 2. The spectrum in Figure 2*a* contains lines from three separate systems: one QSF and FMKs at two velocities. The blue shifted FMK shows [S II] and [O II] doublets of approximately equal strength, while the red shifted FMK is sulfur dominated. Figure 2*b* shows emission from two FMKs. The narrow line at about 6930 Å is due to a cosmic ray. Note also the different noise levels in the two spectra. The background level in Figure 2*b* is typical of the lower levels seen in the images taken with the slit oriented north/south, while that in Figure 2*a* is typical of the higher background seen in the 12 east/west spectra.

The spectra were rebinned in logarithmic wavelength after the flux calibration, making them linear in velocity for the subsequent analysis. Then, for each spatial cross section, each velocity component is found by cross-correlating a spectrum with a rest-frame template and using the shift in pixels between the two to determine the velocity. We used two templates, each a spectrum of delta functions: one consisting of lines for the [N II] doublet and for Hα, and one consisting of lines for [S II], [Ar III], and [O II]. The first allows us to find QSF with velocities between -4000 and 1000 km s^{-1}. The redshifted limit was imposed for the automated routine because of the strong possibility of interference from a blueshifted [S II] line due to an FMK which fell in the same part of the slit. The second template finds FMK emission with velocities between

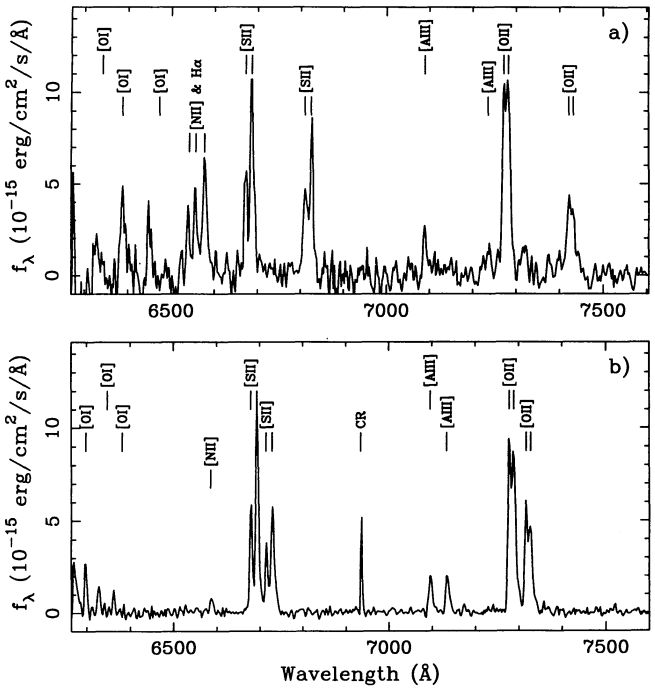

FIG. 2.—Two example spectra of moderate flux. The spectrum in (*a*) contains lines from three separate systems: one QSF and FMKs at two velocities. (*b*) Emission from two FMKs. The narrow line at about 6930 Å is due to a cosmic ray. Note also the different noise levels in the two spectra. The background level in (*b*) is typical of the lower levels seen in the images taken with the slit oriented north/south, while that in (*a*) is typical of the higher background seen in the 12 east/west spectra. The effective aperture size is that of the 1.6 arcsec^{-2} pixel.

$-10{,}000$ and 10,000 km s^{-1}. Although each template contains only the most prominent lines expected, when a system was found we calculated the correct positions for other target lines in our list and recorded fluxes for these lines as well. The complete list of lines was [O I] $\lambda\lambda$6300, 6364, [N II] $\lambda\lambda$6548, 6583, Hα λ6563, [S II] $\lambda\lambda$6717, 6731, [Ar III] λ7136, [Ni II] λ7378, [Ca II] λ7291, [O II] $\lambda\lambda$7320, 7330, and [Fe II] λ7155.

The flux in a line was estimated as the product of the flux in the pixel corresponding to the peak of the line, times the FWHM of the line, i.e., we have modeled the line as a triangle of height equal to the peak flux, with a width of 2 times the FWHM. This was done for computational simplicity to allow an automated procedure. The FWHM equals the cross-correlation peak width determined for each system. Theoretically, this will give a total flux which is 94% of that for a Gaussian of the same peak height and FWHM. We were naturally concerned about the signal-to-noise ratio levels we obtained with this method compared to those we would expect for a Gaussian fit. In our method, the width of the line usually is equal to the instrumental resolution and is always defined by a set of several lines; therefore, the error in the flux estimate comes only from the measurement of the peak flux. The signal-to-noise ratio, S/N, in the flux estimated from the triangular area is therefore the same as that in the peak pixel. For our FWHM, and including the factor of 0.94 between the triangle and Gaussian areas, the S/N of the triangle estimate is 60% that of the ideal Gaussian with no background noise. This situation will be approximately true at high fluxes. We require the minimum peak flux to be at least four times the background noise level for a line to be recorded. At this detection

limit, the sum over the line becomes poorer for the Gaussian, due to the background contribution, and the improvement over the triangle method would be less, but still about 30% over ± 1.5 FWHM. In our spectra, the median flux in the peak pixel in a single FMK [O II] line, is $\sim 18\ \sigma$, giving an error in the flux of about $\pm 6\%$. Furthermore, our analysis generally depends on comparative studies of the summed doublets, and this summed flux is $\sim 25\ \sigma$ for a median pair, or about $\pm 4\%$ for the pair. The QSFs generally are less bright, and the median peak for these lies about 6 σ above the background, giving an error of $\pm 17\%$. These accuracies were considered to be acceptable, and the convenience and ease of automation for the triangle method outweighed the potentially higher sensitivity of the Gaussian. Moreover, the slits often contain multiple knots of emission at different velocities. These systems can be very close together and the resultant spectrum very confused. The example spectra shown in Figure 2 are rather straightforward compared to some of the spectra. Estimating the fluxes of the individual components with a triangular area based on the flux in the peak pixel proved to be very robust in these situations.

The final position on the sky of each optical emission knot was found using the stars scattered across Cas A to convert pixel coordinates along the slit into positions on the sky for each spectrum. This constitutes the third part of our initial analysis. We measured the coordinates of stars from a deep CCD image of Cas A and used pictures of the slit position taken from the monitor to identify unambiguously stars in each slit. We matched these coordinates to the pixels in which the stellar continua fell, and then calculated the position of the central pixel of the slit and its orientation. The slit orientation (north/south or east/west) was quite accurate, but alignment using the star positions gave a considerable improvement over the nominal slit center positions given by the telescope coordinates. The absolute accuracy to which we can reconstruct the slits positions is about ± 1.5 s of arc in either right ascension or declination. The spatial resolution is $0''.64$ pixel^{-1} along the slit, so the relative positions of knots along a slit are determined to within $1''$. The slit width, which also governs the velocity accuracy, is $2''.5$. Our determinations for position and velocity are seen to be repeatable, in that the values found from the east/west oriented spectra are consistent with those from north/south spectra where an image of both types crosses the same knot of emission. Similarly, adjacent north/south spectra may include parts of the same feature. In such cases, velocity estimates differ by $|\Delta v| \sim 120$ km s^{-1}, and on-sky positions vary by $\sim 1''.3$, confirming our error estimates for these parameters.

2.3. *Reliability of the Extraction*

We tested the performance of the extraction routine in two respects: for ability to extract the correct velocities and number of systems from a spectrum, and for reliability of the flux estimate. First, we followed the procedure interactively. With a raw spectrum, the program attempted to fit systems down into the noise, and to prevent this problem, we set noisy regions of the spectrum to zero. We found that a modified spectrum in which we kept pixels with $\gtrsim 4\ \sigma$ above the background noise and set the others to zero gives results that match well the results we get by hand. We also applied the routine to a synthetic spectrum of known signal-to-noise ratio and were satisfied with the reliability of the $\gtrsim 4\ \sigma$ cutoff. Our priority was to select reliable systems rather than to extract every weak system. We tested the flux estimates using all of the single-velocity systems, comparing the estimated flux with the total integrated flux in the line. This was obtained by summing all pixels in a region ± 1.5 times the FWHM. The argon lines in such spectra are the only clear single line available, but we also summed the flux across each line of the well-resolved sulfur doublet to create a second test sample. As stated above, we expect our flux estimate to be 6% lower than a true Gaussian. We find that at high fluxes (above 3.6×10^{-14} ergs cm^{-2} s^{-1}) our flux is 92% of the summed flux, while at low fluxes (below 3.6×10^{-15} ergs cm^{-2} s^{-1}) the flux falls to 76%. At intermediate flux values (from about 1.8×10^{-14} ergs cm^{-2} s^{-1}), our estimates are 90% of the summed flux under the line and our 1 σ scatter is 12%, if we assume that the summed flux measurement has no error of its own. When we assume that the measurement error in summing over the line is about the same as that of our estimated flux (i.e., the error in finding the flux of the peak pixel), then the 1 σ scatter improves by $2^{1/2}$ to 8.5%. Practically speaking, this means that our procedure is performing very much as we expected from the theoretical error determination in relative flux. It is worth noting here that a comparison of the [O I] λ6300 flux distribution with velocity against that of [O I] λ6364 reveals the same pattern at a strength of 3 times (excepting different velocity cutoffs for extreme blueshifts), just as is physically required. This gives us added confidence in our weaker flux determinations, since these two lines were independently determined.

Multiple systems were found as follows. The strongest peak of the cross-correlation function gives the shift in pixels for the system with the strongest intensity. We recorded a flux for every target line as described above. We then set the major lines to zero and repeated the cross-correlation process until all velocity systems were matched and extracted, first for the QSF and then for the FMK template. Flags were set to denote the presence of weak continua or cosmic rays. The final set of systems presented here represent a conservative subset of all the detected systems. We have included only those systems which contain at least two lines detected at the same wavelength shift with a flux in the peak pixel of more than 4 σ above the background.

Uncertainties in the velocities of multiple systems in general are no greater than those of single FMKs. The minimum velocity separation between FMKs in the same slit is determined by the error in absolute velocity introduced by the width of the slit (± 200 km s^{-1}). The error in finding the peak pixel by cross-correlating a template to an arc line spectrum is only 0.16 pixel, corresponding to 16 km s^{-1}, which is negligible compared to the above velocity resolution. The correlation program recognizes peaks separated by as little as 2 pixels. Since the lines of the oxygen doublet are separated by only 4 pixels, multiple systems could be most easily confused in this region; however, in 75% of all systems, the sulfur doublet is also present and pins down the velocity. It is possible to have multiple knots in one slit which have only [O II] lines, but in this case, the systems would be treated as one only if the velocity separation between them was less than ~ 300 km s^{-1}.

Incorrect identification of target lines is fairly unlikely. For instance, in measuring the subsidiary line, [Ca II] λ7290, we have considered potential confusion with lines of the [O II] doublet. The separation between the [O II] lines and the [Ca II] line are 17 and 21 pixels in our spectra. This is not an interval which is matched by the spacing between any template lines, so even a strong [Ca II] line is not likely to be misiden-

tified. Instead, its flux will be estimated at the correct position relative to the major FMK lines of [S II], [O II], and [Ar III]. If [Ca II] emission were present in a sulfur-dominated knot, where the oxygen lines are weak, the [S II] doublet will be matched and the wavelength scale will still be well defined.

2.4. *Summary of Extracted Spectra*

The extraction process described above resulted in 3663 detections of optical emission from FMKs, and 454 detections of [N II] emission from slow-moving knots (QSFs). Some of these detections are parts of a larger physical structure on the sky which was crossed by several spectra. In this sense, our detections are not optical "knots," but elements of emission, but we will continue to refer to them as FMKs and QSFs. The spectral range of our observations allows us to compare the relative fluxes of several important lines for every knot. We have used the relative strengths in the [O II] and [S II] doublets along with density information from the ratio of the [S II] lines to explore abundances, excitation levels, and density in Cas A, details of which follow throughout the text.

Our aim in this study is to be confident in the velocity systems we have found, to compare the relative fluxes within each knot, and to explore general trends in fluxes throughout the remnant. Our identifications of velocity systems are very reliable because we have required our detection program to find more than one line having a minimum signal in the peak pixel of four times the background. We estimated the flux in the line as the area of a triangle, so the S/N of the line is the same as that of the peak pixel (see § 2.2). This S/N is somewhat lower than could have been achieved by Gaussian fitting, but our simple method was found to be very robust in the case of close, multiple systems. The error in the position of an FMK on the sky is $\pm 1''.5$, and the error in the velocity of the system is ± 200 km s^{-1}.

Our average background levels are 2.5×10^{-16} ergs cm^{-2} s^{-1} arcsec^{-2} for the north/south images and 4.4×10^{-16} ergs cm^{-2} s^{-1} arcsec^{-2} for the east/west images. Some of the individual images have background levels lower than these averages; hence, the minimum detected flux in the peak pixel can be less than 4 times the average background. The total flux of an FMK was estimated as the combined sum in both the [O II] and [S II] doublets. These range from 6.0×10^{-15} ergs cm^{-2} s^{-1} to 5.8×10^{-14} ergs cm^{-2} s^{-1}, with a median of 4.1×10^{-14} ergs cm^{-2} s^{-1}. The QSF flux, measured as the flux in [N II] 6583, ranges from 1.9×10^{-15} ergs cm^{-2} s^{-1} to 3.0×10^{-13} ergs cm^{-2} s^{-1}, with a median of 5.0×10^{-15} ergs cm^{-2} s^{-1}. These fluxes represent the flux within a pixel of 1.6 arcsec^2. These also include the systematic factor in flux of 6%, which compensates for the difference in area between a triangle and a Gaussian. The S/N is about 18 for a single FMK [O II] λ7330 line of median flux and about 6 for a QSF [N II] λ6583 line of median flux. Emission from Hα is seen in 30% of QSF. These QSFs are not inherently brighter than those in which no Hα is seen; the [N II] fluxes range from 1.7×10^{-15} ergs cm^{-2} s^{-1} to 1.4×10^{-13} ergs cm^{-2} s^{-1}.

3. KINEMATICS OF CASSIOPEIA A

3.1. *Spherical Expansion Model*

We begin our analysis by assuming spherical expansion for Cas A and then performing a least-squares spherical fit to the data. We allowed five parameters to vary: the radius of the sphere, its displacement from a nominal center in α, δ, and velocity, and the expansion velocity of the shell. We chose for our initial parameters a radius of 1'.7, an expansion velocity of 5000 km s^{-1}, a center at $23^h21^m12^s$, $+58°32'24''$, and zero velocity offset. This position on the sky is the first zero point used by Minkowski (1959) for the center of the circular nebulosity and has become a standard reference for the optical center. We then found the fitted values of the five parameters, corresponding to the lowest value of χ^2 using all the FMK data points. To further refine the fit, we removed the few points (3.5%) from the data set for which the radial distance differed by more than 4 σ from the fitted radius of the shell. These deviant points correspond to material in the jet and to rare knots which lie outside the main shell of Cas A, some of which form small radial filamentary extensions. The fitting program was run again, and the best-fit values from this set became the final values for the model. To complete the model we computed the 1 σ (68%) confidence limits for each parameter. We stepped through a ± 10% range in 0.5% increments for each parameter in turn, allowing all the others to vary until a minimum χ^2 for the step was found. We thus obtained a curve of χ^2 versus value for each parameter, with the minimum being the χ^2 of the best-fit for all parameters. The 1 σ ranges are then taken from the above curves as the parameter values at which the value of $\chi^2 \pm$ has increased by an amount (6.0) corresponding to 1 σ for a five-parameter fit (see Lampton, Margon, & Bowyer 1976 for a fine discussion of parameter estimation; also Avni 1976 and Bevington 1969).

Table 1 summarizes the results of the fit. The radius of the spherical cavity is 1'.741 or $104''.5 \pm 0''.7$, corresponding to a velocity of 5290 ± 90 km s^{-1}. For the thickness of the shell we take the rms scatter about the fitted radius, which is $\pm 5''$, or 260 km s^{-1}, corresponding to only 5% of the radius of the sphere. The radius of the spherical surface is essentially the same as that of the soft X-ray–emitting shell ($105'' \pm 8''$; Fabian et al. 1980). Previous work has established that the optical FMKs of Cas A appear to be part of a freely expanding shell. Transverse velocities, as measured from proper motion studies, are well correlated with angular distance from the center of Cas A and show no significant deceleration over a 29 yr period (VDBK83; VDBK85). Table 2 lists various determinations of the expansion center of Cas A, together with quoted uncertainties and the offsets of each from the nominal geometric center. Figures 3*a*–3*c* show plots of radial velocity v_r, against angular distance, θ, from each of three chosen centers for our sample of FMKs. Figures 3*a* and 3*b* assume optical centers from KVDB76 and the standard reference center, respectively. Figure 3*c* assumes our fit to the expansion center. Plots of this relationship all show the signature of an expanding shell. The improvement in the scatter using the new center is apparent from the figure. Overall, given the quality of our fit, we concluded that the surface at which the FMKs are seen is well described as a sphere with an expansion center offset from zero velocity and from both the geometrical and the proper motion center of the remnant.

TABLE 1

BEST-FIT PARAMETERS OF SPHERICAL EXPANSION MODEL

CENTER OFFSETS[a]				
α	δ	v_c (km s^{-1})	RADIUS	V_{shell} (km s^{-1})
$-9''.5 \pm 0''.7$	$6''.2 \pm 0''.8$	770 ± 40	$104''.5 \pm 0''.7$	5290 ± 90

[a] From Geometric Center and 0 km s^{-1}.

TABLE 2

COMPARISON OF CENTERS IN VARIOUS WAVEBANDS

Reference	Date	Observation Type	α(1950)	δ(1950)	$\Delta\alpha$[a]	$\Delta\delta$[a]
Geometric	...	...	$23^h21^m12^s$	+58°32′24″	0″	0″
Minkowski	1959	Optical	23 21 11.8 ± 0.4	+58 32 16.0 ± 8	−1.6	−8
VDBK	1983	Optical	23 21 11.9 ± 0.1	+58 31 17.6 ± 1	−0.8	−6.4
Fabian et al.....	1980	X-ray	23 21 11	+58 32 40	−7.8	16.0
Tuffs	1986	Radio	23 21 10.2 ± 0.4	+58 32 19.7 ± 4.4	−14.1	−4.3
A&R[b]	1995	Radio	23 21 10.3 ± 0.2	+58 32 25.6 ± 3.1	−13.3	1.6
Reed et al.	1995	Optical[c]	23 21 10.8 ± 0.09	+58 32 32.0 ± 0.8	−9.5	6.2

[a] From Geometric Center.
[b] Anderson & Rudnick 1995.
[c] Results of least-squares spherical fit.

Figure 3*d* presents a similar plot for the slow-moving knots (QSFs), where radial velocity is plotted with respect to distance from our fitted center on the sky. There is no clear signature of an expanding shell. For the purposes of the plot, we have scaled the velocity axis so that 500 km s^{-1} corresponds to 2′ on a justified scale. This seems to give the best correspondence between the QSF map and features of the FMK distribution, but may have no physical significance. In our sample of QSFs, we see a population with an average velocity of −150 km s^{-1}, which includes knots with radial velocities ranging from −4000 to +900 km s^{-1}, although the majority (76%) are blueshifted and at less than 1000 km s^{-1}. Evidence for an *ordered* expansion is very weak, and we see no evidence to support the suggestion (VDBK85) that the QSF form an expanding cloud.

3.2. *Two Hemispheres?*

Braun (1987) has suggested a model for Cas A consisting of approaching and receding hemispheres, each with an expansion center at zero velocity, but with different radii. His model, based on a v_r versus θ plot of the optical data of Minkowski (1959), assigns a radius of 110″ to the approaching hemisphere and 121″ to the receding hemisphere. Braun suggests that these hemispheres may further be identified with the inner and outer radio shells, although the agreement between the radius of the larger hemisphere in his model and the observed radius of the outer radio emission is not good.

We have used our more extensive data set to test Braun's model. If the spherical fit discussed above is allowed to define the true deviance of the data, then the reduced χ^2 for Braun's model is 1.7, indicating that the likelihood of his model's being an accurate description of the data is <0.5%. In a two-hemisphere fit to the data in which the radii are allowed to vary, but the expansion center is fixed at zero velocity, the best-fit has shell radii of 100″ and 107″, and a reduced χ^2 of 1.1. If the expansion center is allowed to vary as well, the two-hemisphere model becomes difficult to distinguish from our original displaced sphere model, with hemisphere radii of 104.″6 and 104.″5 (within the 90% confidence limits of the radius of the displaced sphere model), v_c = 900 km s^{-1} (at 3 σ of the spherical fit), and velocity scales of 52.6 and 48.9 km s^{-1} arcsec^{-1} (at 2 σ of the spherical fit).

This comparison is presented graphically in Figure 4, which shows plots of velocity versus radial distance from the expansion center in the spherical model and Braun's hemispherical model. FMKs which are located to the east of the expansion center are plotted as negative radial distances, while FMKs

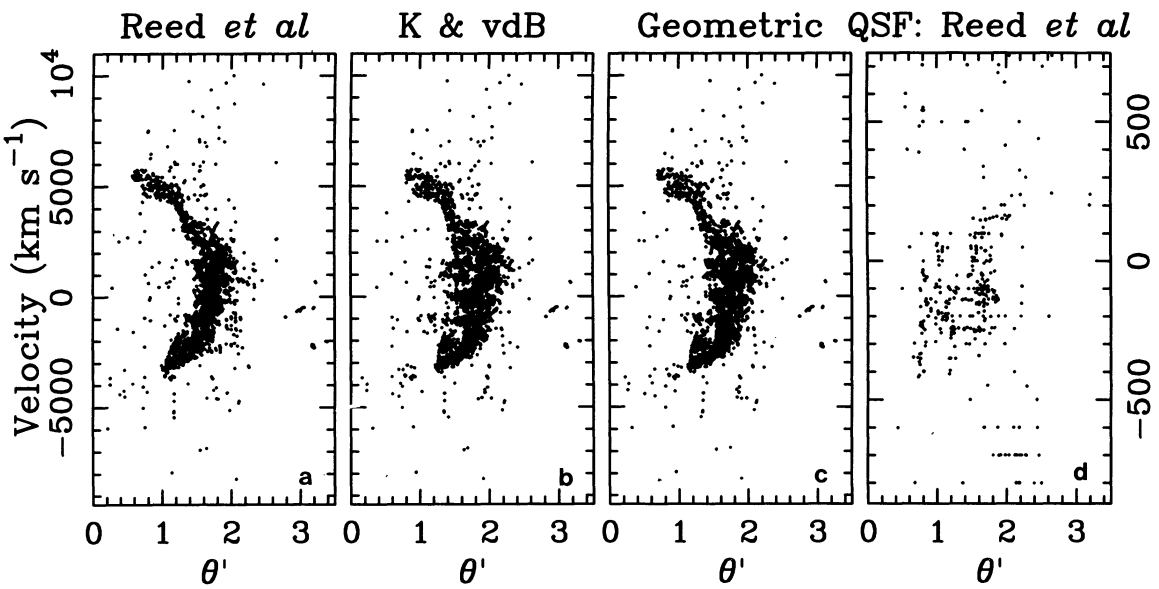

FIG. 3.—Panels (*a*)–(*c*) show plots of radial velocity v_r, against angular distance, θ, from a chosen center for our sample of FMKs, assuming three different expansion centers. Panel (*a*) assumes an optical center as defined by KVDB76. Panel (*b*) assumes the geometric center defined by Minkowski. Panel (*c*) uses a center based on a fit to our data. Plots of this relationship all show the signature of an expanding shell, but the scatter about the arc has been significantly reduced for our fitted center. Panel (*d*) presents a similar plot for the slow-moving knots (QSFs). Here, evidence for an ordered expansion is very weak.

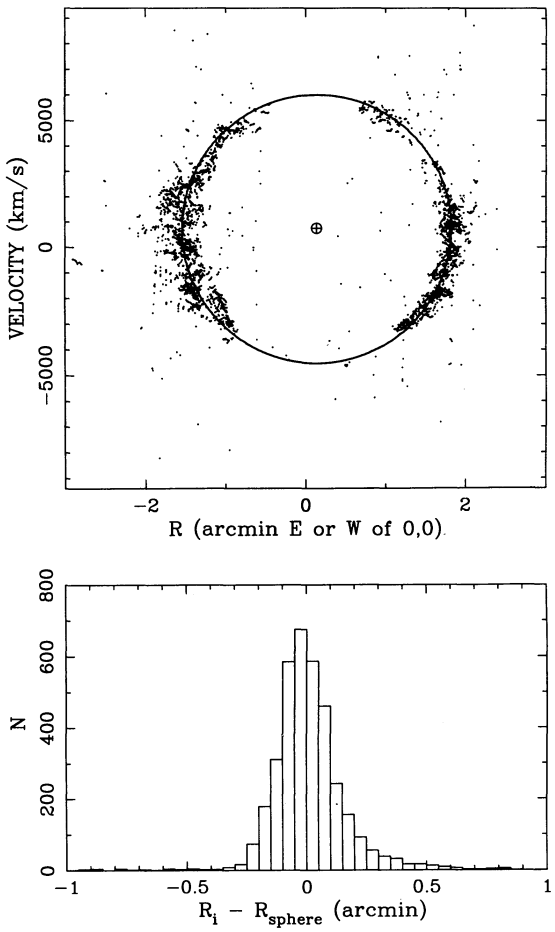

FIG. 4a

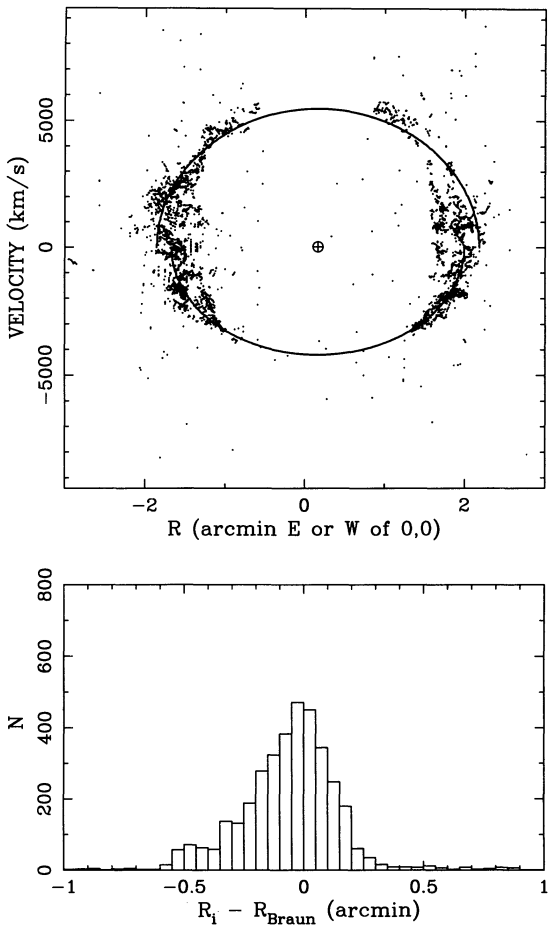

FIG. 4b

FIG. 4.—Comparison of the spherical and hemispherical models with the data. Plots of velocity vs. radial distance from the expansion center are shown for each model. FMKs which are located to the east of the expansion center are plotted as negative radial distances, while FMKs located to the west of center are plotted as positive radial distances. Panel (*a*) shows these data overlaid with our spherical fit. Also shown is a histogram of the differences between the data positions and the spherical fit. Panel (*b*) shows Braun's model overlaid on the same data, together with a histogram of the differences between the data and the two hemisphere model. The comparison of these figures, both in terms of the general appearance of the fit and the shape of the distribution of the residuals, shows that the data are represented much better by our spherical fit.

located to the west of center are plotted as positive radial distances. Figure 4*a* shows these data overlaid with our spherical fit. Also shown is a histogram of the differences between the data positions and the spherical fit. Figure 4*b* shows Braun's model overlaid on the same data, together with a histogram of the differences between the data and the two-hemisphere model. The comparison of these figures, both in terms of the general appearance of the fit and the shape of the distribution of the residuals, shows that the data are represented much better by our spherical fit.

We conclude that there is no optical evidence for a dual-hemisphere model in the velocity structure of Cas A. This leads to a rather significant difference in overall interpretation of the structure of Cas A. In particular, while Braun has suggested that the observed inner and outer radii of Cas A are the line-of-sight superposition of the two hemispheres, we find that the outer radio emission must truly lie beyond (i.e., outside) the inner radio and optical shell.

3.3. *Distance to Cassiopeia A*

The first distance estimates of Cas A were based on Minkowski's early data of ~50 FMKs and ranged from 3.4 ± 0.3 kpc (Minkowski 1959) to 2.8 kpc (van den Bergh 1971). Both estimates were arrived at under the assumption that Cas A consisted of a thin, isotropically expanding envelope, with a limiting radius of 118″ and expansion velocity of 7440 km s^{-1} (Minkowski) or radius 130″ and expansion velocity of 5669 km s^{-1} (van den Bergh). In both cases, the expansion of the shell, $\dot{\theta}$ (in seconds of arc per year) was obtained by fitting a line to the proper motion of each knot versus its distance, θ(″) from the center of the remnant, and using the slope, v_θ/θ to calculate the proper motion at the chosen limiting radius for the expanding shell. The ratio of the radial velocity to the proper motion (in appropriate units) provides the size, in kilometers, of 1″ at the distance of Cas A, and therefore the distance to the remnant. Sakhibov (1980) combined published data from both of the above sources and allowed the central velocity, v_c, to be nonzero, interpreting this offset as translational motion of the nebula. He estimated the distance to be 2.75 ± 0.1 kpc for a v_c of 1000 km s^{-1}, and 4.1 ± 0.9 kpc for a v_c of 400 km s^{-1}, but favored a v_c of 720 km s^{-1}, taken from the average of Minkowski's limiting blueshifted (−6000 km s^{-1}) and redshifted (+7440 km s^{-1}) expansion velocities. The corresponding distance estimate for his favored velocity displacement was

3.1 ± 0.3 kpc. Braun (1987) employed a new method of analysis to determine a distance using published radial velocity and proper motion data. For each knot, the expansion velocity, v_{exp}, the radial velocity, v_r, and the transverse velocity, v_t, are related by $v_{exp}^2 = v_r^2 + v_t^2$, where v_{exp} is assumed constant for all knots in the shell. The transverse velocity, v_t, of a knot is assumed to be given by

$$v_t = \delta \times \left(\frac{v_\theta}{\theta}\right) \times \theta ,$$

where δ is the physical scale (km arcsec^{-1}; δ is proportional to the distance to Cas A), v_θ/θ is the average proper motion per second of arc, and θ is the angular distance of the knot from the center of expansion. If the assumption of uniform expansion is valid, then

$$v_r^2 = v_{exp}^2 - \delta^2\left(\frac{v_\theta}{\theta}\right)^2 \theta^2$$

for all knots. Thus, a plot of v_r^2 versus θ^2 should be linear, with intercept v_{exp}^2, and a slope which is proportional to the square of the distance to Cas A. The error in determining the slope governs the error in this estimate.

Braun (1987) employed this method using the radial velocity data of Minkowski (1959) and the proper motion data and center of VDBK83 and obtained a distance estimate of 2.9 ± 0.1 kpc, where the quoted uncertainly does not include the uncertainty in the proper motion value. He calculated FMK positions relative to the VDBK83 center and zero velocity. We are able to repeat this analysis using our much larger data sample. The results are shown in Figure 5*a*. The value $v_\theta/\theta = (3.26 \pm 0.3) \times 10^{-3}$ yr^{-1} (VDBK83) was calculated for a reference date of 1965. We must scale this for our 1986 observations as a percentage of the remnant lifetime. We will assume that the real explosion date is the Flamsteed date of 1680, but even if the date of 1657 derived from the proper motions (KVDB76) were correct, this introduces only a small error. The scaled proper motion result is then $v_\theta/\theta(1986) = (3.04 \pm 0.3) \times 10^{-3}$ yr^{-1}. If we fit a single line to our data, and use the value $v_\theta/\theta(1986)$, we obtain a distance of 3.7 ± 0.8 kpc, where the uncertainties in the linear fit and in v_θ/θ have been added in quadrature. However, inspection of Figure 5*a* shows that the data are *not* well fitted by a single line. Rather, as Braun noted, the data bifurcate into two branches, corresponding to the approaching and receding faces of the remnant. Figure 5*b* shows the results if we repeat this analysis, but now correct the observed radial velocities using the velocity offset and center on the sky which were determined from the spherical fit discussed in § 3.1. The data now determine a better defined line, which yields a distance to Cas A of 3.4 ± 0.4 kpc, where again uncertainties in the linear fit and in $v_\theta/\theta(1986)$ have been included. The first four entries in Table 3 show the expansion velocities and distance estimates obtained from this method for various choices for the center of expansion. This method is valuable in that it makes no assumption about whether or not deceleration has occurred at some time in the past; however, the errors are large. This is partly due to the outliers arising from material outside the main shell (e.g., the jet), but primarily from the mapping of both negative and positive values of v_r onto the positive v_r^2 axis. Nevertheless, the scatter is smallest for the position and velocity center obtained from our least-squares fit.

A second estimate of the distance can be obtained by combining directly our values for the expansion velocity and shell size with v_θ/θ. Because we use the results of the spherical fit, we use the available data more fully, including the sign of the radial velocity, to arrive at a better estimate of the expansion velocity and size of the spherical shell than was possible for the linear comparison. Here we use $v_\theta/\theta = (3.21 \pm 0.3) \times 10^{-3}$ yr^{-1}, which is the slightly smaller value obtained when the jet material is excluded (KVDB76), since we are now using a

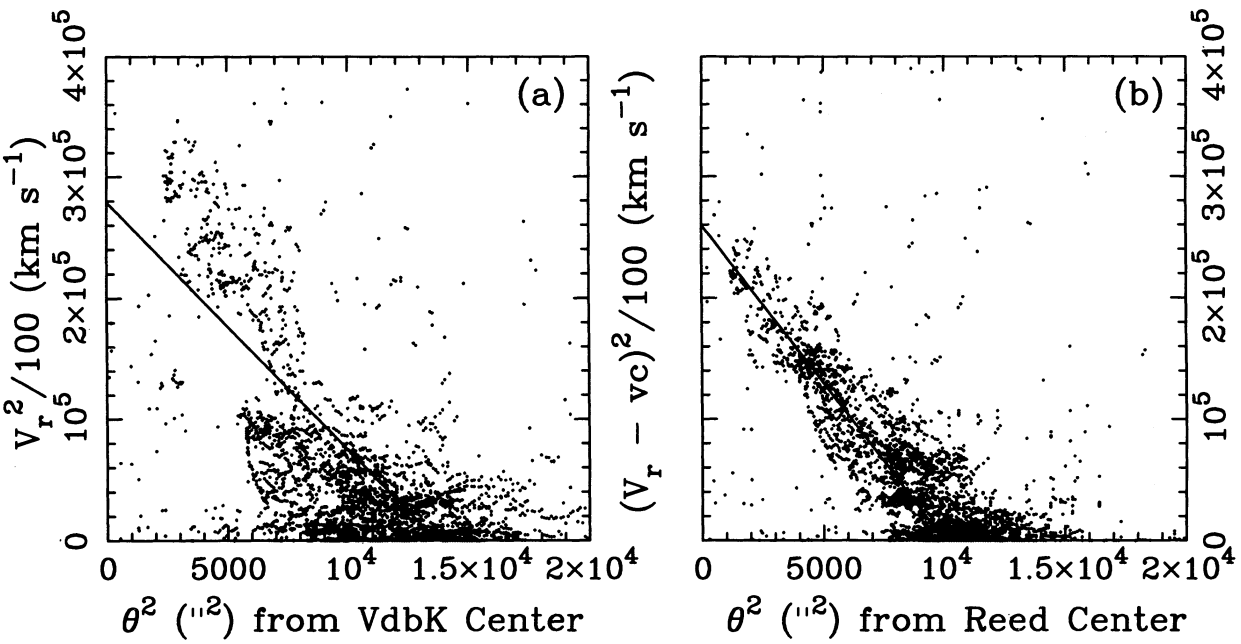

FIG. 5.—Plots of v_r^2 vs. θ^2. In (*a*) we have repeated the method of Braun (1987) using the uncorrected line-of-sight velocity, and the VDBK83 center. Panel (*b*) shows the results when the observed radial velocities are corrected using the velocity offset and center on the sky which were determined from our spherical fit. The data now lie upon a well-defined line. These plots allow a rough estimate of the distance to Cas A (see text).

TABLE 3

COMPARISON OF THE V_{exp} AND DISTANCE ESTIMATES OF THREE METHODS

Method	$(\alpha, \delta)_{center}$	v_c(km s^{-1})	v_{exp}(km s^{-1})	D(kpc)
v_r^2 vs. θ^2	Braun[a]	0	5280	2.9 ± 0.1[b]
v_r^2 vs. θ^2	VDBK	0	5600 ± 1000[c]	3.7 ± 0.8[c]
v_r^2 vs. θ^2	Reed et al.	0	5500 ± 850[c]	3.9 ± 0.6[c]
v_r^2 vs. θ^2	Reed et al.	770	5100 ± 550[c]	3.4 ± 0.4[c]
v_{exp} vs. v_θ	Reed et al.	770	5290 ± 90[d]	3.57 ± 0.06[e] ± 0.3[c]
$R = v_{exp}\, t_{1680}$	Reed et al.	770	5390[f] ± 90[d]	3.33 ± 0.06[e]
$R = v_{exp}\, t_{1680}$	Reed et al.	770	5490[g] ± 90[d]	3.39 ± 0.06[e]

[a] Braun 1987 values from VDBK83 center using Minkowski 1959 data. All others use Reed et al. data.
[b] Error quoted by Braun. Did not include uncertainty in v_θ/θ.
[c] Uncertainty including uncertainty in v_θ/θ VDBK.
[d] Uncertainty from spherical least-squares fit.
[e] Formal uncertainty in fit.
[f] Assuming no deceleration and $v_{opt} = 100$ km s^{-1}.
[g] Assuming no deceleration and $v_{opt} = 200$ km s^{-1}.

velocity and radius determined from our fit, which also excluded these knots. This scales to $v_\theta/\theta(1986) = (2.99 \pm 0.3) \times 10^{-3}$ yr^{-1}. This estimate, which again does *not* assume uniform expansion over the life of the remnant, gives

$$\delta = \frac{v_{exp}}{v_\theta} = \frac{(v_{exp}/\theta_{shell})}{(v_\theta/\theta)} = (5.35 \pm 0.09) \times 10^{11} \text{ km arcsec}^{-1} ,$$

or $D = 3.57 \pm 0.06$ kpc. Using the proper motion scale obtained from data including the jet slightly decreases this distance. The error quoted here represents only propagation of the formal uncertainty in our spherical fit. The full uncertainties are actually larger, $\pm 0.5 \times 10^{11}$ km arcsec^{-1} and ± 0.3 kpc respectively, owing to the 10% uncertainty in the determination of (v_θ/θ) by KVDB76.

An independent determination of the distance to Cas A comes from a comparison of our spherical fit parameters with the 306 yr period between the explosion (as reported by Flamsteed) and the time our observations were obtained. Using the shell radius and expansion velocity from Table 1, we find

$$\delta = (v_{exp} \times t/\theta) = (4.89 \pm 0.09) \times 10^{11} \text{ km arcsec}^{-1} ,$$

or a distance of 3.27 ± 0.06 kpc. This represents a lower limit to the distance to Cas A, because any deceleration of the ejecta would mean that the average expansion velocity is greater than the velocity at the current epoch. Unlike the previous determination, where movement of the optical material in radial and transverse directions was compared, this is a direct comparison of R/v_{exp} versus the time since the explosion. The velocity of the optically emitting material differs from the true velocity of the knot because of the optical shock being driven into it, and this is significant here. As the value of v_{opt} increases the true expansion velocity of the knot increases, and the minimum distance increases. At the same time, as our expected distance goes up, the discrepancy between this and the distance derived from the second method (which is dependent on proper motion) goes down. Thus the two values tend to converge, allowing us to estimate both of these important quantities.

Our two extreme distances are 3.57 kpc from v_{exp}/v_θ and 3.27 kpc from $v_{exp}\, t/\theta$ with no correction for the optical shock. We can reconcile these values if we attribute the difference solely to an 8% deceleration of the FMKs, or solely to a v_{opt} of 440 km s^{-1}. Undoubtedly, however, both effects are important. We will make a plausible compromise by using the average of these, 3.4 kpc, as the "true" distance to Cas A. Bringing the free-expansion minimum distance up to 3.4 kpc implies that the real v_{exp} must be 5500 km s^{-1}, and therefore that the reverse shock into the knot must have a velocity of about 210 km s^{-1}. The remaining difference between the v_{exp}/v_θ distance and 3.4 kpc implies an average deceleration of the FMKs of 4%. In light of our model, it is probable that this slowing occurs abruptly at the shell radius, rather than gradually as the knot travels from the center of expansion. We know that there must be at least a 100 km s^{-1} direct shock into the FMKs, for optical emission of [S II], [O II], and [Ar III] to be seen. A shock of 210 km s^{-1} at the knot face is not at all implausible, when we remember that off-axis shocks will be of lesser velocity. Table 3 includes values of v_{exp} and D for 100 and 200 km s^{-1} shocks into the FMKs. This apportionment reconciles the measurements of the proper motion dependent method with the free-expansion distance and gives us a reasonable estimate of the deceleration of the optical FMKs and of the velocity of the shock being driven into them.

The best distance estimates for the three methods are summarized in the last four lines of Table 3. These estimates of the distance are in a real sense different from one another in their use of the available data. When radial and proper motions are compared, we find that $D = 3.6 \pm 0.3$ kpc, with errors dominated by the uncertainty in (v_θ/θ). We also find that $D \geq 3.33 \pm 0.06$ kpc, where the equality applies when making the additional assumption that the optical ejecta have not been decelerated, and the velocity of the reverse shock into the FMK is at least 100 km s^{-1}. Comparison of these values places a limit of 7% on the difference between the current expansion velocity for these optical knots and the average expansion velocity of these knots since the explosion. However, two considerations have allowed us to narrow the range of this estimate. The knots used in the proper motion study were of necessity those older than 10 yr and therefore probably overestimated the average deceleration in the optical ejecta. Second, the shock into an FMK is likely to have a velocity higher than 100 km s^{-1} considering the dynamics of the interaction. In fact, optical emission seems to be only just possible in Cas A, since it is rare, but continually strengthening and spreading within the remnant (VDBK85). We adopt the average between the distance derived using the proper motion data and that for free-expansion with no correction for the

reverse shock velocity. Because the minimum is well established and the optical shock velocity is known approximately, we favor a distance estimate of $3.4^{+0.3}_{-0.1}$ kpc. Given these arguments, the deceleration of the FMKs must be of order 4% or less, and the reverse shock of order 200 km s^{-1}. This study confirms that Cas A's optical emission comes from ejecta which has been slowed hardly at all by interactions with the environment.

4. THE CIRCUMSTELLAR MEDIUM AROUND CASSIOPEIA A

The velocity displacement in our spherical fit might in principle arise from a high space velocity of the progenitor or an asymmetrical explosion. However, neither a 770 km s^{-1} space velocity for a W-R star nor a 25% dipole asymmetry in the velocity distribution of SN ejecta seem very plausible. It is also important to note that the QSFs have a strongly asymmetrical distribution, where 76% have blueshifted radial velocities. This suggests instead that the difference between the front and back faces of Cas A is due to a difference in the medium with which the expanding SNR is interacting. Studies of the inferred deceleration of the radio filaments as a function of position in Cas A (Tuffs 1986; Anderson & Rudnick 1995) also indicate that there exists a significant variation in the density around the remnant as a function of azimuth, both for the inner radio emission and for the outer, diffuse radio ring. The data overall suggest that Cas A is interacting with higher density material on its near and west sides than elsewhere.

4.1. *Models of Cassiopeia A*

The shell structure which Cas A currently shows could have arisen directly from the momentum of the expanding ejecta acting on the surrounding medium or could have arisen during the evolution of the progenitor star, thus predating the SN. Figure 6 shows a schematic diagram of our model of Cas A, applying to either case, in which the final shell is off center with respect to the expansion center of the SN ejecta. In this diagram, the radius of the symmetric sphere is given as R_0. The parameter γ represents the fractional displacement of the site of the explosion from the current center of the shell, which can be calculated from the velocity parameters given by our spherical fit:

$$\gamma = \frac{\Delta v_c}{v_{\rm sphere}} = \frac{770 \text{ km s}^{-1}}{5290 \text{ km s}^{-1}} = 0.146 .$$

In addition, our fitted center on the sky is displaced by 8".7 west and 12".6 north of the expansion center determined from proper motions of the FMKs (VDBK83). We will assume that this displacement measures the magnitude of the asymmetry in Cas A in the plane of the sky, although radio data indicate a stronger east to west change in the deceleration of radio clumps (Tuffs 1986). Adopting a distance to Cas A of 3.4 kpc, the approximately equal offsets of $\sim$15" northwest on the sky and away from us (770 km s^{-1} = 15".2) imply a physical distance of about 1×10^{13} km between the center of the spherical cavity and the assumed center of the explosion. This increases γ to 0.2. This asymmetry corresponds to a ratio for the back and front distances of

$$\frac{R_b}{R_f} = \frac{R_0(1+\gamma)}{R_0(1-\gamma)} = 1.50 .$$

We have determined R_0 to be 104".5 (1.72 pc), and therefore the distances between the center of expansion and the extreme faces are $R_f = 1.38$ pc and $R_b = 2.06$ pc at the distance of Cas A. The radii *directly* along the line of sight (where $\gamma = 0.146$) are $R_f = 1.47$ pc and $R_b = 1.97$ pc. We have examined the approximate density change required to give rise to the greater shell asymmetry for both of the above basic evolutionary pictures.

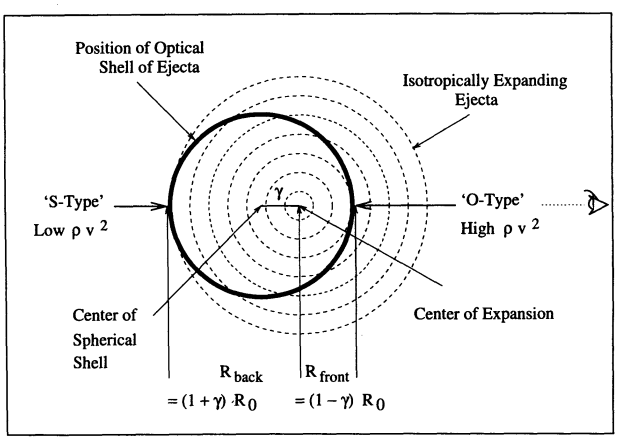

FIG. 6.—A schematic diagram of our model of Cas A, in which the final shell is off center with respect to the expansion center of the SN ejecta. In this diagram, γ represents the fractional displacement of the site of the explosion from the current center of the shell. Knots strong in [O II] predominate on the near side, and those strong in [S II] are seen on the far side of the remnant.

4.1.1. *Expansion of Ejecta into a Density Gradient*

The first and simplest hypothesis to explain the asymmetry of Cas A is that the explosion occurred within a smooth medium with a density gradient, and that the ejecta have created the off-center sphere. The shape of the resulting shell can be approximated as a sphere with its center displaced along the direction of the gradient.

The mass profile is thought to be very steep for the leading ejecta (e.g., $\rho \propto v_{\rm ej}^{-12}$; Chevalier 1982). We used a mass profile which was cut off at $v_{\rm max} = 10{,}000$ km s^{-1} at the leading edge and had the form $v_{\rm ej}^{\alpha}$ from v_0 to $v_{\rm max}$ for the inner profile of the ejecta, where $\alpha = 10$. The parameter α has little effect on the integrated momentum, which is concentrated at $v_{\rm max}$. For example, if $\alpha = 1$, the fraction of the mass having an expansion velocity greater than $\frac{1}{2}v_{\rm max}$ is already $\frac{7}{8}$ of the total ejecta. We have already shown that the minimum velocity for ejecta which has reached the shell, $v_0 = R_0/t$, is about 5300 km s^{-1}. The expansion of the resulting composite shell is taken to be the radio expansion velocity, 1800 km s^{-1} (Tuffs 1986).

Three cases are considered: the uniform density which could give rise to a symmetric sphere; the two-density case of a SN explosion at a boundary layer; and an exponential density gradient which is parallel to the line of sight. In the first case, the uniform density giving the symmetric sphere of radius $R_0 = 1.72$ pc was found to be $n_0 = 10$ cm^{-3} for each solar mass of ejecta which has become part of the shell. The total mass swept up, $M_{\rm sw}$, from this medium of n_0, would be $4.1 \times M_{\rm ej}(M_\odot)$. However, we have shown that an off-center expansion much better describes Cas A, and that along the line of greatest asymmetry, $R_f = R_0(1-\gamma) = 1.38$ pc, and $R_b = R_0(1+\gamma) = 2.06$ pc. The simplest two-density case is that where the center of the explosion occurred at a boundary between two layers. This of course would result in two

hemispheres of unequal size. Although this is not the case for Cas A, it provides an estimate of the minimum density contrast. The two values of the density were found to be $n_{0,f} = 20$ cm^{-3} $\times M_{ej}(M_\odot)$ for the blueshifted side, and $n_{0,b} = 4$ cm^{-3} $\times M_{ej}(M_\odot)$ for the redshifted side. Then $M_{sw,f} = 2.6 \times M_{ej}(M_\odot)$, $M_{sw,b} = 2.5 \times M_{ej}(M_\odot)$, and the total is $5.1 \times M_{ej}(M_\odot)$. Finally, we chose a more realistic, exponential distribution of density and modeled the shell with a radius, R_θ, which varied as a function of angle, again scaling parameters of radius and velocity as above. This could create a nearly spherical cavity about a displaced center. We calculated a central density of $n_c = 11$ cm^{-3} $\times M_{ej}(M_\odot)$, and scale height, $H = 0.85R_0$, or 6.4×10^{18} cm (2.1 pc). The total mass swept up was $4.9\ M_\odot/M_{ej}(M_\odot)$. The implied density contrasts derived from these models (for the opposing media at each extreme) are $\sim$5.5 from back to front of Cas A for a two-medium boundary and $\sim$10.4 for an exponential gradient having the characteristics described above. The approximate densities for the current swept-up shell, consisting of ambient material and ejecta combined, are of order 45 cm^{-3} $\times M_{ej}(M_\odot)$ for the uniform medium, 25, and 120 cm^{-3} $\times M_{ej}(M_\odot)$ in the case of the two-medium boundary, and ranging from 15 to 95 cm^{-3} $\times M_{ej}(M_\odot)$ for the exponential density gradient, a factor of 6 times from back to front.

The estimated X-ray–emitting mass around Cas A, between 15 and 30 $M_\odot$ (Murray et al. 1979; Fabian et al. 1980; Jansen et al. 1988), is in good agreement with the above mass estimates if of order 2–4 $M_\odot$ of ejecta have reached the inner shell. X-ray spectra suggest that the bulk of the X-ray–emitting material came from the progenitor star. The outer radio and X-ray emission mark the position of the blast wave, and this high-temperature outer X-ray emission comes from material with approximately solar abundances (Becker et al. 1979; Jansen et al. 1988). The total amount of ambient material within this outer shock radius (150″) is $14 \times M_{ej}(M_\odot)$ for $n_0 = 10$ cm^{-3} $\times M_{ej}(M_\odot)$, again of the correct order even if we were to assume that all the ambient material within the outer shock radius has been shocked to X-ray temperatures. Although our mass estimates are in basic agreement, analysis of the radio knots suggests that Cas A cannot be expanding as a SNR directly into a smooth medium (Dickel et al. 1989). These calculations therefore provide only a rough estimate of the densities required if a slow composite shell of swept-up circumstellar matter and ejecta has been formed by the action of the ejecta of Cas A. Nevertheless, they give an indication that the amount of mass surrounding Cas A would need to have been at least of order 10 $M_\odot$ at the time of the explosion, and they show the approximate density contrasts which are suggested by the velocity asymmetry.

4.1.2. *Expansion of Ejecta into a Presupernova Bubble*

A second possible explanation of Cas A's underlying spherical geometry is that stellar mass loss of the progenitor via a stellar wind created an off-center cavity into which the SNR evolved. Such off-center bubbles are common around O and W-R stars (e.g., Miller & Chu 1993). For example, published images of NGC 7635 and NGC 2359 (Johnson 1980; Dufour 1991) show $\gamma = 0.5$ and $\gamma = 0.3$, respectively. This type of asymmetry must be due to a density gradient in the medium upon which the wind acts, rather than to any asymmetry in the wind itself, since the bubble is driven by the isotropic pressure inside it (Garcia-Segura & Maclow 1993). In comparison, Cas A ($\gamma = 0.2$) is a fairly symmetrical object.

We begin by assuming that the current asymmetry of Cas A is representative of the off-center cavity into which Cas A evolved and ask what sort of density gradient is required to produce a bubble with $\gamma = 0.2$. For the luminosity-driven case, a dimensional analysis, where the parameters are the mechanical luminosity of the stellar wind, $\dot{M}v^2$, the time, t, and the constant ambient density, n_0, gives the expression

$$R(t) \propto \left(\frac{L_{\rm wind}\, t^3}{n_0}\right)^{1/5} .$$

A full analysis of a stellar wind expanding into a constant density medium, including cooling effects, is found in Weaver et al. (1977), who find that this proportionality holds for early and intermediate stages of the bubble lifetime. In our case we are concerned with the difference in bubble size between the front and back faces. To get an estimate for the density gradient in the region into which the bubble expanded, we compare the density required to produce a bubble having radius $R_b = (1 + \gamma)R_0$ with the density required to produce a bubble having $R_f = (1 - \gamma)R_0$. Here R_f and R_b are distances from the explosion center to the front and back faces of the remnant, respectively. This gives

$$\frac{n_{0,f}}{n_{0,b}} = \left(\frac{R_b}{R_f}\right)^5 = \left(\frac{1+\gamma}{1-\gamma}\right)^5 \sim 7.6 ,$$

where $n_{0,f}$ and $n_{0,b}$, respectively, are the average densities into which the front and back faces of the bubble expanded. If we consider the momentum of the stellar wind, $\dot{M}vt$, to be driving the expansion against a background density, n_0 (although this is thought to be a less likely scenario for a symmetric bubble), then

$$R(t) \propto \left(\frac{Mvt}{n_0}\right)^{1/2} ,$$

(Shore 1992). Equating the momenta at each side of the bubble gives the ratio

$$\frac{n_{0,f}}{n_{0,b}} = \left(\frac{R_b}{R_f}\right)^4 \sim 5.1 .$$

This calculation shows that a density change of 5–8 times from front to back over the diameter of Cas A could have led to a preexisting cavity of the observed shape. This ratio should also be present in the density of the final shell which the SNR later encounters.

The calculations in this and the previous section indicate that the global asymmetry of Cas A can be explained if the ejecta is encountering material on the front face which is $\sim$5 times more dense than material on the back face. Further, this calculation is insensitive to the exact details of the circumstellar environment into which Cas A evolved.

4.2. *Global Variations across Cassiopeia A: Composition or Pressure?*

One of the most interesting, and potentially most important, observations about the optical knots in Cas A has been the wide range of abundances implied by the observed line ratios. Knowledge of the distribution of real differences of composition could greatly improve our models of SN explosions and of their massive progenitors. If large enough regions of ejecta

consist of material from coherent regions of the progenitor, we might expect to see some relationship between the inferred abundances of knots and their positions and kinematics in our large sample. However, we have found that the conditions of excitation in Cas A (e.g., ejecta velocity, shell velocity, and shell density) vary in systematic ways within the remnant. These are further complicated by the ringlike distribution of ejecta on the surface of the sphere (Paper II). These variations will have an effect on emission-line ratios and will complicate efforts to sort out real differences in abundances among the knots.

4.2.1. *Global Trends Predicted by the Model*

Based on our off-center shell model, we expect conditions on the front face of the remnant to differ from conditions on the back face. Fast-moving knots on the front face are moving more slowly than on the back face and should arise from deeper within the SN. Previous investigators have looked for correlations between composition and velocity in the FMKs. VDBK85 concluded that knots showing strong [O III] lines have lower velocities than those showing strong [S II] lines and that, at a marginally significant level, the [O III] population is decelerating more rapidly. Kirshner & Chevalier (1977) and Chevalier & Kirshner (1978, 1979) discussed spectrophotometry of ~25 FMKs in Cas A, covering the wavelength range from 4000 Å to 7500 Å for suspected sulfur-rich knots, or from 3500 Å to 7000 Å for suspected oxygen-rich knots. They concluded that the composition of knots does differ, with sulfur, argon, and calcium related to each other, but that knots show no trend of composition with velocity. They suggested that Cas A has been mixed either during the explosion, or because of Rayleigh-Taylor instabilities which may have left inverted regions of gas with different abundances.

In addition, pressures on the front face should be higher than pressures on the back face, because it is in this direction that the expanding ejecta has encountered higher density material. At the current epoch we are seeing ejecta interacting with a shell of material that has already been swept up and accelerated by the supernova explosion. Based on our discussion of the geometry of the remnant (§ 3.1) we assume that the outer X-ray and radio emission arise behind the blast wave at the outer edge of this shell and that the very bright radio and X-ray emission are associated with the dense inner region of the shell.

In order to evaluate changes in pressure around the remnant, we need to know not only the motions of ejecta as a function of position, but also need an estimate of the expansion velocity of the shell. Such estimates can be obtained from radio proper motion data, which show an overall expansion velocity of order 1800 km s^{-1} but vary according to the density of the medium into which the shell is expanding (Anderson & Rudnick 1994). To obtain a rough estimate of the motion of the shell, we assume that the velocity of the shell varies around the remnant in the same way as the ejecta. This seems a generally plausible assumption, in that the near side, which encountered a denser medium and should therefore be expanding more slowly, is also the side where the deeper, slower ejecta are currently interacting.

Making this assumption, the ratio of shell velocities on the front and back face is the same as the ratio of ejecta velocities on the two faces. The difference between the ejecta and shell velocities can then be written as $\Delta v = v_{ej} - v_{sh}$ and is given by

$$\Delta v_f = (1 - \gamma)(\langle v_{ej} \rangle - \langle v_{sh} \rangle) ,$$

and

$$\Delta v_b = (1 + \gamma)(\langle v_{ej} \rangle - \langle v_{sh} \rangle) .$$

The ram pressure driving shocks into the FMKs on each face will then be given by

$$\frac{P_f}{P_b} = \frac{n_{0,f}}{n_{0,b}} \left(\frac{\Delta v_f}{\Delta v_b} \right)^2 = \frac{n_{0,f}}{n_{0,b}} \left(\frac{1 - \gamma}{1 + \gamma} \right)^2 = 0.44 \frac{n_{0,f}}{n_{0,b}} \sim 2.2 ,$$

where we have assumed that $n_{0,f}/n_{0,b} \sim 5$.

4.2.2. *Trends in the* [S II] *Ratio*

We can look for the effects of such a front/back asymmetry in the remnant in our data. Table 4 presents the average properties of knots in five velocity slices going from the front to the back of the remnant. Columns (1) and (2) show the velocity range for each slice. The last column contains the number of FMKs in each slice, while column (5) shows the number of FMKs for which both [S II] lines were detected. Averages for several parameters relating [O II] and [S II] strength, [S II] ratio, and inferred electron density are also shown. The importance of each in interpreting Cas A is discussed below.

Since the postshock temperature at which [S II] emission is formed is not a strong function of shock parameters, the values of n_e inferred from the [S II] line ratio give a direct measure of the ram pressure driving the shock into a clump of ejecta. In principle, this should allow us to measure directly the pressure gradient from the front to the back of the remnant. In practice, observational uncertainties limit the utility of such a measurement. Most optical knots are close to the high density limit for the [S II] doublet: $n_{crit} = 2 \times 10^{-3}$ cm^{-3}. Therefore for most FMKs the ratio of the [S II] lines spans a range of only 0.4 to 0.55. Small changes in [S II] ratio in this region correspond to large changes in n_e, so the errors here are particularly significant. Despite this fact, we do see marginal evidence for a trend in the [S II] ratio between the front and back. If we fit a line to

TABLE 4

PARAMETRS FOR VELOCITY SLICES

v_1 (km s^{-1}) (1)	v_2 (km s^{-1}) (2)	$\langle \eta \rangle$ (3)	$\langle \log n_e \rangle$ (cm^{-3}) (4)	N_{SII}^a (5)	$\langle$Flux$\rangle$ (10^{-13} ergs cm^{-2} s^{-1}) (6)	S-Type (7)	I-Type (8)	O-Type (9)	N (10)
−10000	−2000	0.73	3.75	224	1.54	0.22	0.29	0.50	606
−2000	0	0.68	3.41	515	1.14	0.27	0.36	0.37	1135
0	2000	0.54	3.31	605	1.26	0.42	0.39	0.18	1062
2000	4000	0.55	3.43	297	0.91	0.53	0.21	0.26	488
4000	10000	0.49	3.47	240	0.70	0.60	0.19	0.21	372

[a] Knots containing [S II] emission.

the "measurements" of n_e in Table 4, we infer a factor of ~ 2 contrast in $\langle P \rangle$ between the two faces. This is similar to our estimate above.

4.2.3. *Trends in the Relative Strengths of* [O II] *and* [S II]

A much stronger contrast between the front and back faces of the remnant is seen when considering the parameter $\eta =$ [O II]/([O II] + [S II]). This parameter is especially well determined because it relates the strengths of the four strongest lines in our spectra in a ratio which is less uncertain than the strength of a single line. The range spanned is $\eta = 0.2$–0.8 for the [S II]–containing FMKs. A value of $\eta = 0$ or 1, of course indicates that either [O II] or [S II] were below our threshold for detection. The η measurement also probes the distribution of knots in which *no* [S II] is seen. This distribution shows that many of the extreme O-type knots are found at the largest blueshifts and form a "skin" which lies outside the [S II]–containing knots.

Table 4 gives average values of η for each of our five velocity bins. In addition, we broke our population of FMKs into knots of three types. Knots with $\eta \geq 0.8$ we refer to as "O-type" (31% of FMKs); knots with $\eta \leq 0.5$ are referred to as "S-type" (38% of FMKs); and knots with $0.5 < \eta < 0.8$ are referred to as "intermediate" or "I-type" (31% of FMKs). Knots showing only [O II] emission comprise a significant fraction of the knots detected: 25% of all FMKs, and 80% of knots denoted as O-type. Knots with only [S II] emission are rarer, comprising 8% of the overall population. While many of the O-type knots which show no detectable [S II] emission are relatively bright, S-type knots lacking [O II] emission are usually faint. Generally speaking, most knots lacking detectable [O II] emission can probably be explained as more "normal" knots where [O II] just fails to exceed the detection limit. Strong [O II] knots without [S II] emission, on the other hand, seem to require that [S II] is truly significantly depressed with respect to [O II].

The average η increases for slices taken from back to front of the remnant. The distribution within each velocity bin is shown in Figure 7. These distributions are not Gaussian, having sizable numbers of knots in each slice which have values of $\eta = 0$ or $\eta = 1$, with the latter shown as the value $N(1)$. Therefore, uncertainties in these values are not quoted. The trend of η with velocity is also shown in the increasing fraction of O-type knots which fall in the blue-shifted slices. In slice 5, at the far side of Cas A, S-type knots constitute 60% of all FMKs, whereas in slice 1, 50% of all the knots are O-type, and in fact, 40% of the FMKs in this slice have no detectable [S II] emission at all. Figure 8 shows a more finely binned sample of the fraction of S-type, I-type, and O-type FMKs in each of 14 velocity slices across Cas A. We see that O-type knots make up 73% of the flux in the blueshifted layer, but only 20% of the knots with greatest redshift.

It is tempting to assume that such variations in η are dominated by variations in the relative abundances of O and S. However, the pressure gradient across the remnant complicates such a straightforward interpretation. While the [S II] line ratio is relatively insensitive to density for $n_e \sim 10^4$ cm^{-3} (well above n_{crit}), the total intensity of the sum of the lines is not. This implies that η is sensitive to electron density. For plausible ranges in density, a factor of 2.5 variation in pressure between the front and back faces will result in a variation of about 0.25 in η (where the S/O ratio is adjusted to match the observed average value of η). This is in reasonably good agree-

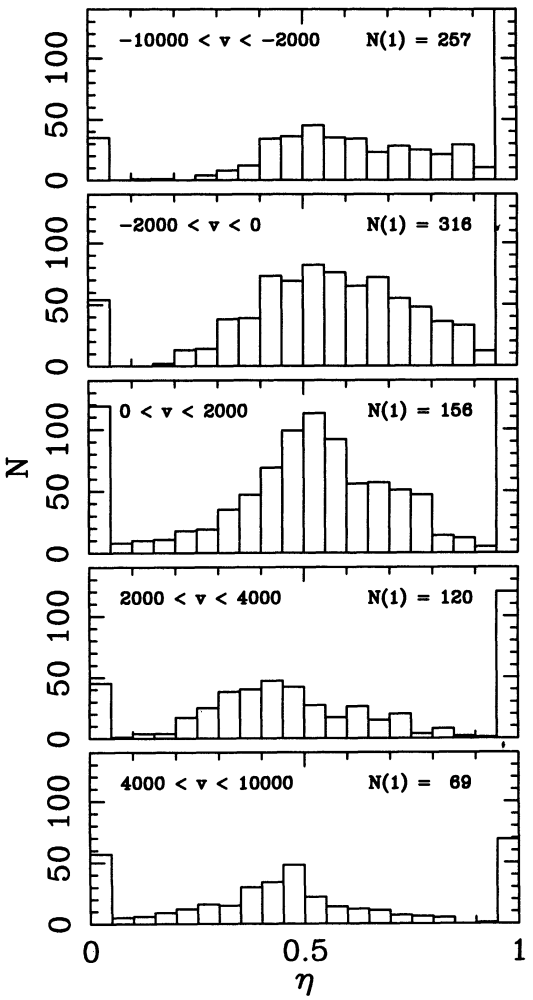

FIG. 7.—The distribution of relative strengths of [O II] and [S II] emission within each of five radial velocity bins. This fraction for each knot is expressed as $\eta =$ [O II]/([O II] + [S II]). The average η increases for slices taken from back to front of the remnant. These distributions are not Gaussian, having sizable numbers of knots at $\eta = 0$ and at $\eta = 1$, so uncertainties in these values are not quoted.

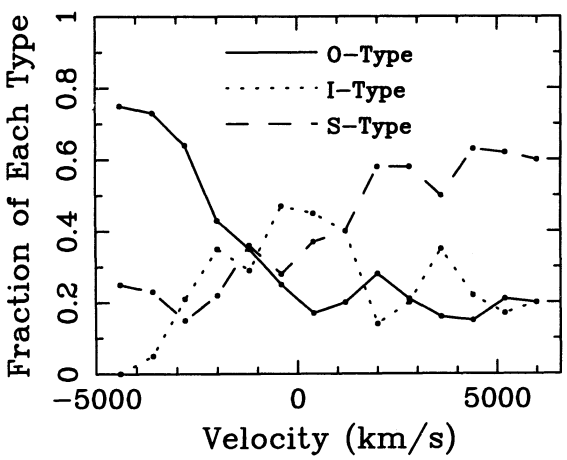

FIG. 8.—A more finely binned sample of the fraction of S-type, I-type, and O-type FMKs in each of 14 velocity slices across Cas A. We see that O-type knots make up 73% of the flux in the blueshifted layer, but only 20% of the knots with greatest redshift.

ment with the observed range in $\langle\eta\rangle$ between the two faces of 0.48 to 0.73 for all knots, or 0.32 to 0.51 when neglecting knots showing only [O II] or only [S II].

Our conclusion based on this analysis is that the pronounced front to back asymmetry in the ratio [O II]/([O II] + [S II]) is *not* primarily due to a systematic difference in abundance between the two faces. Rather, it is due to differences in the degree of collisional deexcitation of [S II] between the front high pressure face and the back lower pressure face. No systematic variations in the relative abundances of O and S between the two faces are demanded by our analysis so far. This conclusion is supported by the lack of systematic variations in [Ar III]/[O II] within the remnant since, while the Ar abundance might be expected to follow the S abundance, the ratio of [Ar III]/[O II] is less sensitive to density.

Chevalier & Kirshner (1978, 1979) include positions and radial velocities for many of their knots, enabling us to place these on our three-dimensional map. We have also used the listed line ratios to calculate an η for each knot and find these to match our values within our errors. They use the [S II] doublet at λ4070, when available, to arrive at the S/O by mass. Their values for S/O by mass for one knot in the jet and one knot apparently at the front face, are quite low (<0.1, which is roughly of cosmic level) even though η is about 0.45 in either case, placing it just into the S-type category in our nomenclature. Both are in presumed high-density regions. The values of η from their data correlate somewhat with the [S II] ratios when these are present. Knots of very low η (<0.3) tend to have [S II] ratios greater than 0.65, or inferred $n_e < 3000$ cm^{-3}. The number of knots studied is small, so that only one knot (in the SW) which falls into our O-type class has a quoted [S II] ratio, but this is at the high-density limit. In the other two knots of this type, unfortunately, the spectral range missed the red [O II] doublet, but their study is in general agreement with our own. With spectroscopic data spanning only 6250–7600 Å, we cannot positively state that there is no front-to-back trend in composition, but the weight of evidence makes a change in pressure the most likely interpretation. We wish to make it clear that we are *not* ruling out knot to knot variations in abundance as discussed by CK, but rather find the observed *ordered* change of [O II]/[S II] with radial velocity can be explained by pressure differences alone.

It is less clear that the concentration of "O-only" knots on the front face of Cas A can be interpreted in this way. Assuming reasonable upper limits for the strength of [S II] in these knots, we require densities of order 1–2 $\times$ 10^5 cm^{-3} on the very front face. This in turn would require pressures on the front face that are probably at least a factor of 10 higher than the back face. This is not an implausible suggestion, given that the average pressure on the front face is already a factor of $\sim$3 higher than the back face. This is especially true given that the "O-only" knots are strongly concentrated in a single feature (Paper II). Overall, it is natural to view the "O-only" knots as an extension of the trend in η, which tracks the pressure difference between the front and back face.

We also note that [O II] and [S II] are formed in different parts of the postshock cooling region, and that if the column depth of postshock material is low enough, then the postshock [S II] zone may not be fully formed. This possibility could be explored by relating an exceptionally high [O II]/[S II] ratio to inferred age of a knot. There does in fact appear to be a good correlation between regions where new knots have been seen to appear (VDBK85) with the locus of "O-only" FMKs from our study. This supports the possibility that the "O-only" knots may be newly shocked clumps of ejecta in which the postshock [S II] region has yet to form. Given the speed at which knots evolve, it will be interesting in the coming years to see whether our population of "O-only" knots begins to show [S II] emission. This possibility that extreme O-type knots may have incomplete cooling and recombination regions could also be addressed by using the ratio of [O I] to [O II] to infer the existence or absence of the coolest portions of the postshock region (cf. Hester, Parker, & Dufour 1983; Raymond et al. 1988). Unfortunately, while we do have [O I] in our spectra of knots on the back face of the remnant, the [O I] λ6300 line is blueshifted off the end of our spectra for approach velocities greater than about 2000 km s^{-1}, leaving only the weaker [O I] λ6364 line. This excludes the major concentration of "O-only" knots at $v \sim -3000$ km s^{-1}.

In Paper II we discuss the details of the peculiar distribution of the knots in Cas A over the surface of the remnant. Here we point out only that the "O-only" knots are concentrated in a well-defined ring on the surface of the remnant and speculate that the mechanism responsible for the formation of this and other rings could also affect the excitation conditions in the FMKs.

Despite all this, it is still interesting to speculate on what the implications would be if we were to ascribe the concentration of "O-only" knots to a real difference in the relative abundances of S and O. In this case, the S/O ratio is *lowest* on the front face of the remnant, which corresponds in turn to material coming from deepest within the SN explosion. This is opposite the expected trend within the progenitor, in which lighter oxygen-rich material is outside sulfur-rich material.

5. CONCLUSIONS

The weight of observational evidence from optical, radio, and X-ray wavelengths suggests that the general form of the Cas A supernova remnant is due to the expansion of ejecta from a position displaced from the center of the remnant toward us and slightly to the NW. Cas A is well fitted by a spherical shell of radius 104".5 in which the velocity center has been redshifted by 770 km s^{-1}. This expansion of the ejecta from a displaced center accounts for the observed radial velocity difference at the front and back faces. We have calculated the distance to Cas A using first the combined radial velocity and proper motion data and then the assumed date of the explosion. We find it to be $3.4^{+0.3}_{-0.1}$ kpc. Thus the shell radius for the remnant is 5.3 $\times$ 10^{18} cm (1.7 pc), and the distance scale is very nearly 1' pc^{-1}. The nearly free-expansion of the FMKs, which show a deceleration of less than 4%, in combination with the displaced expansion center, implies that material from deeper within the stellar envelope (whether this has been mixed or not) interacts with the near face of the SNR shell, while outer material interacts with the far face.

The explanation for the global asymmetry in velocity appears to lie in a density asymmetry in the circumstellar material, which may or may not have been distributed in a shell that predates the SN. The change with redshift of the [O II] strength relative to [S II], and the change in the electron density, also suggest that the pressures encountered by the FMKs on the near side of Cas A are greater than those on the far side. These pressures may be high enough to have completely suppressed [S II] emission in some knots on the near face and are certainly high enough that [S II] intensities cannot be used as a reliable indicator of chemical abundances in the

ejecta. However, the suppression of the [S II] lines relative to [O II] has itself allowed us to characterize the global pressure variation. The asymmetry in the QSF distribution gives further strong evidence for a systematic variation in the amount of circumstellar material. This is in accord with radio observations (Anderson & Rudnick 1995).

Simple numerical models of our proposed scenario suggest that many solar masses of circumstellar material surrounded Cas A's progenitor at the time of the explosion. X-ray spectra suggest that the bulk of this material came from the progenitor star. The outer radio and X-ray emission mark the position of the blast wave, and this outer X-ray emission comes from material with approximately solar abundances. At the inner emission radius, the fastest ejecta from the progenitor have already run into and become part of the circumstellar shell, creating a mix of enriched and photospheric material there.

Our kinematic studies strongly support the idea that the optical FMKs are freely expanding, whereas the radio observations show that the remnant shell at the same radius certainly is not (Anderson & Rudnick 1994). The locus of the optical emission itself seems to be expanding only very slowly (CK79; van den Bergh 1971; VDBK83). The strong deceleration of the ejecta at the interface sets up classic conditions for Rayleigh-Taylor instabilities, which may explain the secondary features of Cas A. Among these are the protruding radio bow shocks (Braun et al. 1987), the strong radio emission at the inner radius, and the optical rings of emission. The large velocity difference between the FMKs and the shell implies reverse shock velocities which are too high for optical emission. However, we believe that the optical emission arises primarily where ejecta interacts with low density regions at the edges of holes in the shell, and thus that the optical FMKs are only a very small part of the ejecta of Cas A. The nature of the shell, with its voids and filaments, therefore seems to create variable shock conditions across Cas A which govern whether X-ray or optical emission is seen. This model has ramifications for the X-ray asymmetry (seen by Markert et al. 1983 and Holt et al. 1995), for the QSFs at both inner and outer radii, and for the observable evolution of the remnant. All these points must be examined in the context of the optical rings. We will discuss these features in depth in Paper II.

This work was supported at Arizona State University by NASA/JPL contracts 959289 and 959329 and Caltech contract PC064528. The authors would like to acknowledge useful discussions with R. Harmon.

REFERENCES

Anderson, M. C., & Rudnick, L. 1995, ApJ, submitted
Ashworth, W. B. 1980, J. Hist. Astr., 11, 1
Avni, Y. 1976, ApJ, 210, 642
Baade, W., & Minkowski, R. 1954, ApJ, 119, 206
Becker, R. H., Holt, S. S., Smith, B. W., White, N. E., Boldt, E. A., Mushotzsky, R. F., & Serlemitsos, P. J. 1979, ApJ, 234, L73
Bell, A. R. 1977, MNRAS, 179, 573
Bevington, P. R. 1969, Data Reduction and Error Analysis for the Physical Sciences (New York: McGraw-Hill)
Braun, R. 1987, A&A, 171, 233
Braun, R., Gull, S. F., & Perley, R. A. 1987, Nature, 327, 395
Chevalier, R. A. 1976, ApJ, 208, 826
———. 1982, ApJ, 259, 302
Chevalier, R. A., & Kirshner, R. P. 1978, ApJ, 219, 931
———. 1979, ApJ, 233, 154
Dickel, J. R., Eilek, J. A., Jones, E. M., & Reynolds, S. P. 1989, ApJS, 70, 497
Dufour, R. J. 1989, Rev. Mexicana Astron. Astrof., 18, 87
Fabian, A. C., Willingale, R., Pye, J. P., Murray, S. S., & Fabbiano, G. 1980, MNRAS, 193, 175
Fesen, R. A., Becker, R. H., & Blair, W. P. 1987, ApJ, 313, 378
Fesen, R. A., Becker, R. H., & Goodrich, R. W. 1988, ApJ, 329, L89
Garcia-Segura, G., & Mac Low, M-M. 1993, in Massive Stars and Their Lives in the Interstellar Medium, ed. J. P. Cassinelli & E. B. Churchwell (ASP Conf. Ser., 35), 354
Hester, J. J., Parker, A. R., & Dufour, R. J. 1983, ApJ, 273, 219
Holt, S. S., Gotthelf, E. V., Tsunemi, H., & Negoro, H. 1995, PASJ, submitted
Jansen, F., Smith, A., Bleeker, J. A. M., de Korte, P. A. J., Peacock, A., & White, N. E. 1988, ApJ, 331, 949
Johnson, H. M. 1980, ApJ, 235, 66
Kamper, K., & van den Bergh, S. 1976, ApJS, 32, 351
Kirshner, R. P., & Chevalier, R. A. 1977, ApJ, 218, 142
Lampton, M., Margon, B., & Bowyer, S. 1976, ApJ, 208, 177
Markert, T. H., Canizares, C. R., Clark, G. W., & Winkler, P. F. 1983, ApJ, 268, 134
Miller, G. J., & Chu, Y.-H. 1993, ApJS, 85, 137
Minkowski, R. 1959, in Paris Symposium on Radio Astronomy, ed. R. N. Bracewell (Palo Alto: Stanford Univ. Press), 315
Murray, S. S., Fabbiano, G., Fabian, A. C., Epstein, A., & Giacconi, R. 1979, ApJ, 119, 206
Oke, J. B., & Gunn, J. E. 1982, ApJ, 218, 767
———. 1983, ApJ, 266, 713
Peimbert, M. 1971, ApJ, 170, 261
Peimbert, M., & van den Bergh, S. 1971, ApJ, 167, 223
Raymond, J. C., Hester, J. J., Cox, D. P., Blair, W. P., Fesen, R. A., & Gull, T. R. 1988, ApJ, 324, 869
Reed, J. E., Fabian, A. C., Winkler, P. F., & Hester, J. J. 1991, BAAS, 23, 1, 826
Reed, J. E., Hester, J. J., & Winkler, P. F. 1995, ApJ, submitted (Paper II)
Reed, J. E., Winkler, P. F., & Fabian, A. C. 1989, in Supernovae, ed. S. E. Woosley (New York: Springer-Verlag), 649
Ryle, M., & Smith, F. G. 1948, Nature, 162, 462
Sakhibov, F. K. 1980, Soviet Astr. Letters, 6, 56
Searle, L. 1971, ApJ, 168, 41
Shore, S. N. 1992, An Introduction to Astrophysical Hydrodynamics (New York: Academic), 158
Tuffs, R. J. 1986, MNRAS, 219, 13
van den Bergh, S. 1971, ApJ, 165, 457
van den Bergh, S., & Dodd, W. W. 1970, ApJ, 162, 485
van den Bergh, S., & Kamper, K. 1983, ApJ, 268, 129 (VDBK83)
———. 1985, ApJ, 293, 537 (VDBK85)
Weaver, R., Castor, J., McCray, R., Shapiro, P., & Moore, R. 1977, ApJ, 218, 377; erratum, 220, 742